

# Finite Element Simulation of Concrete-Filled Double-Skin Tube Columns Subjected to Postearthquake Fires

R. Imani, A.M.ASCE<sup>1</sup>; G. Mosqueda, A.M.ASCE<sup>2</sup>; and M. Bruneau, F.ASCE<sup>3</sup>

**Abstract:** Detailed finite-element (FE) analyses were conducted using commercial software to simulate the behavior of concrete-filled double-skin tube (CFDST) columns subjected to postearthquake fires. The main goal of these simulations was to replicate results from a series of experiments that first subjected CFDST columns to different levels of seismic damage by applying cyclic lateral loading, and then fire testing of the same specimens in a furnace. The numerical simulations paralleled the experiments in the loading sequence. Different material models and modeling techniques were assessed in terms of reproducing experimental observations including local failure modes such as steel tube buckling. Results from the cyclic loading simulations including residual deformations were maintained as initial conditions for the subsequent thermal-stress analysis to simulate the fire testing phase of the experiments. A sequentially coupled nonlinear thermal-stress analysis was conducted on the models of CFDST columns to study the effects of exposure to a standard fire (time-temperature) curve. Numerical simulations using material properties adopted from European general rules for structural fire design provided a reasonable comparison to experimental results for both during and postfire situations. DOI: 10.1061/(ASCE)ST.1943-541X.0001301. © 2015 American Society of Civil Engineers.

**Author keywords:** Fire following earthquake; Concrete-filled double-skin tube columns; Finite-element analysis; Composite columns; Multihazard design; Seismic performance; Fire resistance; Postearthquake fire resistance; Seismic effects.

## Introduction

Concrete-filled steel tube (CFST) columns have been shown to be a promising multihazard resistant structural system exhibiting high performance for different types of extreme events. Several past studies have demonstrated their desirable seismic performance (Hajjar 2000; Marson and Bruneau 2004; Han and Yang 2005), while a number of separate studies have addressed their fire resistance (Kodur 1998; Han 2001; Han et al. 2003; Hong and Varma 2009; Moliner et al. 2013). More recently, ductile concrete-filled double-skin tube (CFDST) columns, with concrete between an outer and inner steel tube, have also been demonstrated to behave satisfactorily under separate seismic loading (Zhao and Grzebieta 2002; Han et al. 2004; Uenaka et al. 2008) and fire conditions (Yang and Han 2008; Lu et al. 2010, 2011).

Building on this past observed desirable performance, Imani et al. (2014) conducted a series of experiments on CFDST columns to study their behavior under postearthquake fire scenarios, an important area of research given that significant conflagrations after earthquakes have occurred in the past (e.g., Scawthorn et al. 2005), that losses from fires after earthquakes can exceed those from the shaking itself [National Oceanic and Atmospheric Administration (NOAA) 1972], and that, in more recent earthquakes, numerous separate fires confined to single structures have caused significant

damage (Cousins and Smith 2004; Scawthorn 2008). This paper investigates, using finite-element (FE) analysis, the effectiveness of different material models and analysis techniques in replicating the experimental results reported by Imani et al. (2014) and highlights some of the challenges in modeling the sequentially combined seismic and fire effects.

## Summary of Experimental Program

Three nominally identical CFDST column specimens were evaluated in a postearthquake fire scenario. Two of the three specimens were first subjected to quasi-static cyclic lateral loads, imposing varying degrees of lateral drift to simulate two different seismic events [(1) moderate damage level (Specimen S1), and (2) high damage level (Specimen S2)] before being exposed to fire. Specimen S3 was not subjected to simulated seismic loading to serve as a reference. Fig. 1(a) shows the dimensions of the specimen cross section.

Fig. 1(b) shows the cyclic loading setup, in which cantilever CFDST columns were subjected to a constant axial load in the range of 310–360 kN using a posttensioning rod, and to lateral cyclic loading. Under cyclic lateral loading, Specimens S1 and S2 were pushed to the maximum drift of 6–6.5% with different residual drifts of 1.4 and 3.9% for moderate and high damage levels, respectively. Local buckling of the outer steel tube occurred near the fixed bottom end of both specimens from the simulated seismic loading.

The undamaged and damaged columns were then subjected to the same fire tests in accordance with the standard ASTM E119-12a (ASTM 2012) temperature–time curve while sustaining an axial load until the column failed due to global buckling. Fig. 1(c) shows a photo of Specimen S3 in the vertical furnace used for the tests. As shown in Fig. 1(d), compression was applied to the column specimen by eight force-controlled hydraulic actuators displacing a so-called sliding bottom support beam while the top beam

<sup>1</sup>Graduate Research Assistant, Dept. of Civil, Structural, and Environmental Engineering, Univ. at Buffalo, Buffalo, NY 14260 (corresponding author). E-mail: rezaiman@buffalo.edu

<sup>2</sup>Associate Professor, Dept. of Structural Engineering, Univ. of California, La Jolla, CA 92093. E-mail: gmosqueda@ucsd.edu

<sup>3</sup>Professor, Dept. of Civil, Structural, and Environmental Engineering, Univ. at Buffalo, Buffalo, NY 14260. E-mail: bruneau@buffalo.edu

Note. This manuscript was submitted on September 19, 2014; approved on January 30, 2015; published online on March 23, 2015. Discussion period open until August 23, 2015; separate discussions must be submitted for individual papers. This paper is part of the *Journal of Structural Engineering*, © ASCE, ISSN 0733-9445/04015055(15)/\$25.00.

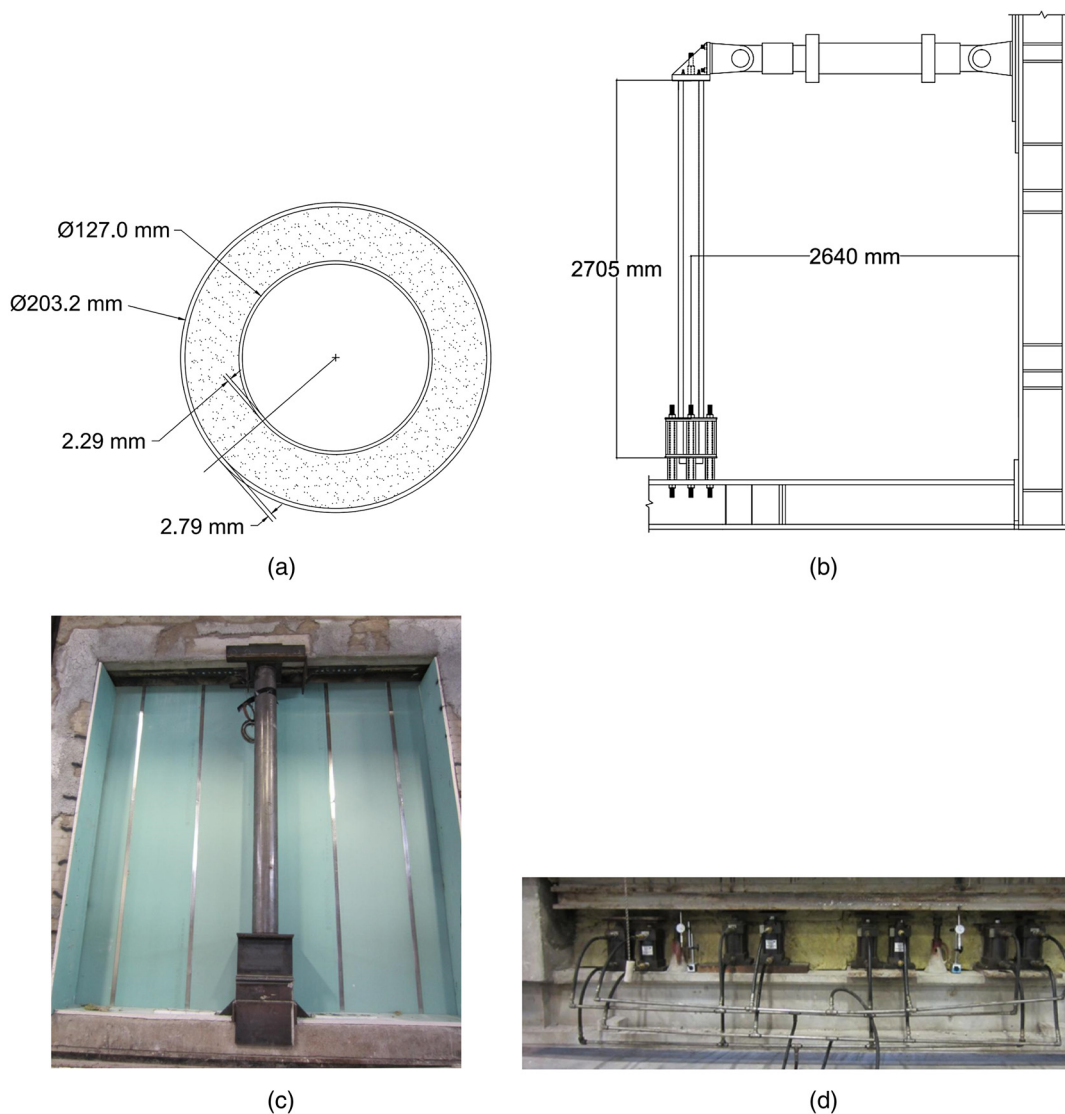


**Fig. 1.** Description of experimental test setup: (a) specimen cross-sectional dimensions; (b) setup for cyclic loading; (c) vertical furnace used for fire tests; (d) hydraulic actuators used to apply axial loads and mechanical gages used for manual reading of axial extension

was fixed. Further details on specimen installation, load application mechanism, and furnace specifics are presented in Imani et al. (2014).

All three specimens failed due to global buckling with fire resistance times of about 65 min for Specimens S3 and S1, and 60 min for Specimen S2. Local buckling of the outer tubes from the fire effects was also observed near the top end of the specimens, due to the thermal expansion and separation from the concrete. Photos of the damaged specimens in different cyclic loading and fire tests are presented along with the simulation results in the relevant sections of this paper.

Overall, the results showed marginal differences in the fire resistance of the three specimens, providing evidence for the resilient performance of these columns under postearthquake fire scenarios. Although beyond the scope of this paper, an additional quasi-static cyclic loading test was conducted on the specimen that had been exposed to fire without any prior damage, to investigate the behavior of the column subjected to seismic loads after the fire test. Again, differences in behavior were modest, except for a 5.7% drop in strength attributed to permanent degradation in material properties due to fire (Imani 2014).

## Simulation of the Cyclic Tests

### Finite-Element Models

Numerical models of CFDST columns were built in *ABAQUS*, with the steel material model based on the stress–strain data measured from uniaxial tension tests. Two coupons were extracted from remaining sections of each of the inner and outer tubes used to construct the three specimens for a total of 12 coupons. Figs. 2(a and b) show the results from tensile tests conducted on different coupons for the inner and outer tubes. A bilinear elastic–plastic model with linear kinematic hardening was fitted to the data with noticeably different values for the inner and outer tubes. The respective yield and maximum tensile strength values based on the average measurements are 303 and 365 MPa for the inner tube, and 344 and 400 MPa for the outer tube [Figs. 2(a and b)]. These values were used in the cyclic testing simulations for all of the specimens. Elastic modulus of 200,000 MPa and Poisson’s ratio of 0.3 were also used for the steel material.

The concrete within the columns was modeled using the damaged plasticity material in *ABAQUS* with compressive strength,

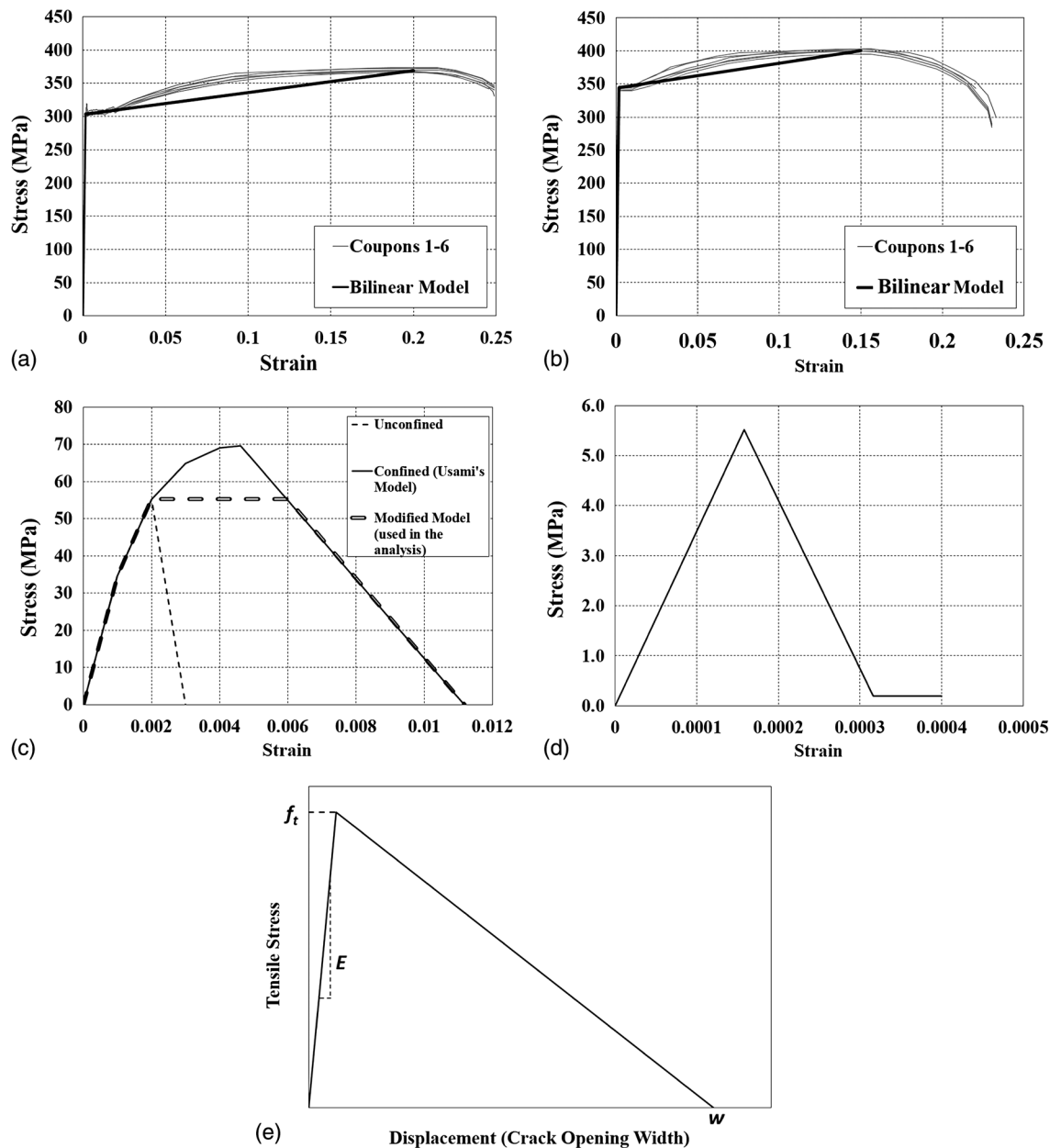


**Fig. 2.** Uniaxial stress–strain relationship used for the material models of steel and concrete: (a) inner tube (with coupon results); (b) outer tube (with coupon results); (c) concrete in compression (used for FE–CDP and FE–CDP–DS); (d) concrete in tension (used for FE–CDP); (e) concrete in tension (used in FE–W)

$f'_c$ , measured from cylinder tests. Cylinders casted on the construction day and tested on the same day as the cyclic tests showed average compression strength values of 55 and 60 MPa for Specimens S1 (first cyclic test) and S2 (second cyclic test), respectively. The initial stiffness for the linear elastic portion of the uniaxial compressive stress–strain curve was calculated based on the equation given in ACI 318-11 (ACI 2011), namely  $E_c = 57,000\sqrt{f'_c}$ , where  $f'_c$  is in units of pounds per square inch, which gives values of 35,149 and 36,659 MPa for Specimens S1 and S2, respectively. Poisson’s ratio for concrete was assumed to be 0.2.

Many researchers (e.g., Mander et al. 1988; Usami et al. 2001; Sakino et al. 2004) have shown that concrete confined by a circular steel tube can exhibit increased strength and ductility. The software *ABAQUS* can capture the increase in the compressive strength due

to confinement but not the added ductility. Therefore, the unconfined stress–strain curve was modified to account for added ductility, using the Usami et al. (2001) stress–strain relationship for confined concrete, by adding a plateau to the stress–strain curve of unconfined concrete, enhancing its ductility to be the same as that of the Usami et al. (2001) model [Fig. 2(c)].

In tension, the concrete strength,  $f_t$ , was assumed equal to 10% of the compressive strength, while the elastic modulus remained equal to the one used for compression. The postpeak behavior was modeled with a linear descending branch, after the cracking strain (strain at the end of elastic region), and maintains a residual strength of  $0.1f_t$  until, conservatively, only twice that strain [Fig. 2(d)]. This residual tensile strength does not have any physical significance and was selected to be slightly above zero to facilitate the computational process.

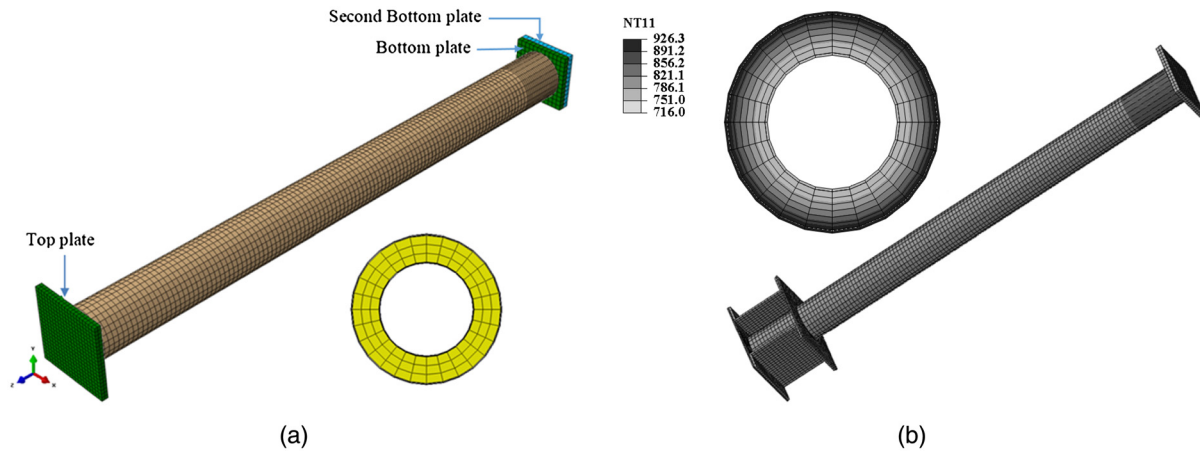


**Fig. 3.** Finite-element models built for the numerical simulations: (a) model for cyclic loading; (b) model for thermal stress analysis with heat transfer analysis results for cross section of Specimen S3

Damage parameters needed for the damaged plasticity model were calculated based on the stress-strain curves given in Figs. 2(c and d) for compression and tension. The strain corresponding to the maximum stress in compression and tension are defined as  $\varepsilon_{f'_c}$  and  $\varepsilon_{f_t}$ . The damage parameters for compression and tension ( $d_c$  and  $d_t$ ) for a given strain value,  $\varepsilon$ , were assumed equal to zero if  $\varepsilon \leq \varepsilon_{f'_c}$  or  $f_t$ . For  $\varepsilon > \varepsilon_{f'_c}$  or  $f_t$ , the damage parameters were calculated as  $d_c = 1 - \sigma_\varepsilon / f'_c$  and  $d_t = 1 - \sigma_\varepsilon / f_t$ , where  $\sigma_\varepsilon$  is the value of stress corresponding to the strain,  $\varepsilon$ , in the compressive or tensile uniaxial stress-strain curve.

Fig. 3(a) shows the FE model built for the cyclic analyses of Specimens S1 and S2. The concrete core was modeled using eight-node solid (i.e., C3D8R) elements while the inner and outer steel tubes were modeled with four-node shell (i.e., S4R) elements. The default hourglass control method in *ABAQUS* was used to control the hourglass modes that might occur in linear elements using the reduced integration method. A nonuniform mesh pattern was used for the model, with smaller element sizes in the area close to the fixed end of the column, where local buckling of the outer tube is expected. The average size of the concrete [three-dimensional (3D) solid] elements in the coarse and fine areas were about  $20 \times 20 \times 20$  and  $10 \times 10 \times 10$  mm, respectively. Similarly for the steel shell elements, the mesh sizes were about  $20 \times 20$  and  $10 \times 10$  mm.

The bottom plate of the column specimen was also modeled and numerically tied to both the inner and outer tubes in the FE model, and a top plate was only tied to the outer tube, such as to replicate the experimental conditions (inner tube was not welded to the top plate due to construction constraints). The interaction at the steel-concrete interface was defined with a hard contact (allowing separation of the surfaces) in the normal direction, and a coulomb friction model in the tangent direction, with a friction coefficient of 0.25. Values of 0.20 to 0.3 have been typically used and shown to provide acceptable results compared to experiments (Johansson and Gylltoft 2001; Espinos et al. 2010).

To simplify the numerical model, loads and boundary conditions were defined with some slight differences compared to the test setup. First, the axial load was applied as a pressure to the central part of the top and bottom plates of the column instead of modeling the posttensioning bar. Second, the column base connection was simplified by removing the additional (built-up) box section, which was used in the experimental setup to protect the base beam. To account for the flexibility of the built-up box section

captured in the cyclic tests, a second plate was modeled just below the bottom plate of the column [Fig. 3(a)] and was kept elastic to act as the base beam of the experimental setup. The two plates were connected by a hard contact model allowing separation of the surfaces with the bolt load feature from *ABAQUS* used to capture the rotational resistance. Push-over analyses were conducted before the cyclic loading simulation to calibrate the flexibility of the base connection for each specimen based on the results from the cyclic tests. This model is referred to as the FE-CDP model [as it uses the concrete damaged plasticity (CDP) model] in the remainder of this paper.

### Push-Over and Cyclic Loading Analysis of Specimen S1

The push-over analysis of the FE-CDP model of Specimen S1 was conducted, as follows: (1) apply prestress load to the bolts, (2) apply axial load of 311 kN as pressure to the column's top and bottom plates, and (3) apply a monotonic displacement to cause a drift ratio of 6.5%.

Fig. 4 shows the final results from the push-over analysis of Specimen S1 (after calibration for the base flexibility) along with the experimental results from the cyclic testing of the column. The final calibrated model with added flexibility at the base has an

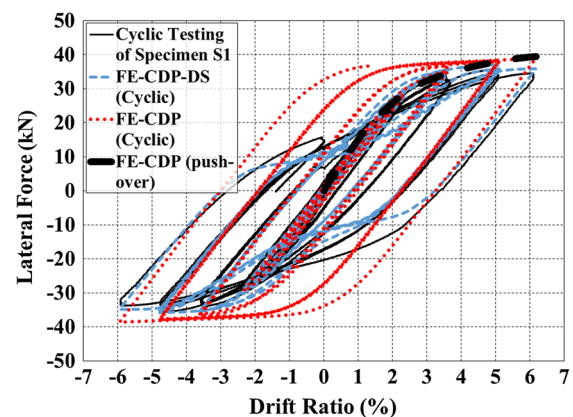


**Fig. 4.** Numerical simulation of the cyclic loading of Specimen S1 using FE-CDP and FE-CDP-DS models

initial lateral stiffness of 0.6 kN/mm, compared to 0.7 kN/mm for the fixed base model (a 10.2% difference).

The lateral force versus drift curve obtained from push-over analysis encloses the experimental cycles and adequately predicts the lateral resisting force at increasing drift ratio. The push-over curve gives lateral force values slightly larger than the experiment for the large displacement amplitudes (i.e., at 5 and 6% drift ratio). This difference is attributed to minor strength degradation in the specimen after going through repeated cycles of relatively large displacements that caused slight local buckling to develop at the base of the outer steel tube.

The FE–CDP model of Specimen S1 with calibrated base flexibility was then subjected to the displacement protocol recorded from the cyclic testing of the column. Fig. 4 shows the lateral force versus drift results from the initial FE analysis. The model provided acceptable stiffness and strength predictions but failed to capture the pinching of the hysteretic curves for the CFDST column under cyclic loading. At the drift ratios of 5 and 6%, the model was also not capable of capturing the strength degradation caused by the local buckling of the steel tube.

Local buckling of the outer steel tube plays an important role in the formation of pinching in the hysteretic curves of cyclically loaded CFDST columns. It occurs on the compression side of the column, especially after having previously stretched and plastically elongated in tension during loading in the reversed direction. Since the concrete core in CFDST columns provides a bearing support for the tubes (thus delaying the occurrence of local buckling), the formation of tensile cracks and their opening and closing in subsequent cycles can affect the amount of strain of the outer tube. More stretching as the cracks open leads to more severe buckling under reverse loading. To account for these effects, the concrete material model needs to capture the initiation and growth of tensile cracks expected to form in that region of the concrete core.

As can be inferred from Fig. 4, the damaged plasticity model used for concrete was not able to accurately simulate tensile cracking in concrete and replicate how the opening and closing of tensile cracks impact pinching behavior in hysteretic curves. This issue was also reported by Goto et al. (2010) in a similar study on numerical modeling of concrete filled columns, because the damaged plasticity model is approximate in terms of its tensile behavior since isotropic plasticity is assumed in tension.

To resolve this problem, Goto et al. (2010) proposed a modification to the model by inserting a horizontal discrete crack (Chen 2007) at the expected crack location identified by a preliminary analysis (in the case of a cantilever column, the major tensile crack occurs in the vicinity of the fixed base). A hard contact was modeled between the two separate concrete surfaces at the horizontal crack to be able to simulate the opening and closing behavior. In the tangent direction, the friction between the two concrete surfaces was modeled using a friction coefficient of 1.0 based on ACI (2011) recommendations. The effectiveness of the proposed solution was verified by comparison with experimental results of different CFT columns (Goto et al. 2010).

In a similar study, Goto et al. (2012) showed that using additional discrete cracks (two or three instead of one) can improve the accuracy of the results for rectangular CFST columns. However, for circular columns, a single crack appeared to be sufficient and was used in the research reported in this paper to avoid further computational challenges from the multiple contact surfaces.

In an attempt to better replicate the experimental results of Specimen S1 (specifically the pinching behavior of the hysteretic curves), the FE–CDP model was modified in two ways. First, the stress–strain curve used for the concrete material in tension was

replaced with a stress–displacement curve (assumed to be equivalent to the crack opening), which, according to the *ABAQUS* documentation, is effective in decreasing the mesh sensitivity of the results for the elements that reach the softening branch of the concrete material's tensile behavior. The stress–displacement curve used in the research reported in this paper was determined using the stress–strain relationship defined previously and the average element size of the concrete model used in the research reported in this paper. With this approach, displacement (crack opening,  $u_{cr}$ ) is related to the equivalent plastic strain by  $\varepsilon^{pl} = u_{cr}/l_0$ , where  $l_0$  is the concrete element length. The damage parameters for the tension side, previously defined as a function of equivalent plastic strain, were also changed to be a function of displacement.

Second, considering that the modified concrete model was still incapable of simulating the crack opening and closing behavior, a discrete crack was inserted at the end of the concrete core close to the base, where the stress contour lines showed the maximum tensile stress values. The crack was modeled by cutting the concrete core along a horizontal plane just above the base and defining an interaction, with the properties mentioned previously, between the two concrete surfaces. This model is referred to as the FE–CDP–DS model (where the term DS is used to indicate a discrete crack) in the remainder of this paper.

Fig. 4 shows the lateral force versus drift ratio results for the cyclic loading of the FE–CDP–DS model of Specimen S1. Results show a much closer agreement to the experimental data because of the improved capability of the modified model to capture local buckling of the steel tube, resulting in the pinching of the hysteretic curves of the CFDST column. The hysteresis curves also show small strength degradations in the cycles at drift amplitudes of 5 and 6.2%. This is also in agreement with the experimental results, supporting the fact that the opening and closing of the tensile cracks in concrete facilitates the local buckling of the steel tube, which then causes strength degradation.

Despite the more severe pinching seen in the hysteresis curves, the FE–CDP–DS model was deemed to provide sufficiently accurate results and was considered acceptable for the FE analysis simulation of the behavior of CFDST columns under postearthquake fire scenarios. However, to investigate if the modeling approach could be further improved, additional analyses were conducted using the program *LS-DYNA*, where instead of inserting discrete cracks at predetermined locations, a different concrete model capable of simulating the behavior of tensile cracks was used. As such, the concrete core was modeled using the Winfrith concrete material, which better simulates the tensile behavior of concrete by attempting to regularize the strain softening in tension through parameters accounting for crack opening width, fracture energy, and aggregate size. The material model flows plastically as a result of failure in compression, but is capable of simulating tensile cracking with up to three orthogonal crack planes per element (Broadhouse and Neilson 1987; Schwer 2011).

To provide a complete set of parameters for the Winfrith model in *LS-DYNA*, aside from the maximum compressive strength, elastic modulus, and tensile strength (assumed equal to the values used in the *ABAQUS* model), the maximum aggregate size was selected to be 6.35 mm, as in the concrete mixture used in the specimen construction. A new stress–displacement (crack opening width) relationship was defined for the behavior of concrete in tension according to the procedure presented in a study by Schwer (2011) on the performance of the Winfrith concrete model. In this procedure [Fig. 2(e)], the stress–displacement relationship starts with a linear elastic branch, going from zero tensile stress to the tensile strength,  $f_t$ , and descends with another linear branch that goes back to zero tensile stress at the crack opening width of  $w$ .

Defining the area under the stress–displacement curve as the specific fracture energy,  $G_F$ , the crack opening width for the zero tensile stress ( $w$ ) can be calculated from

$$w = \frac{2G_F}{f_t} \quad (1)$$

Recommended values for the specific fracture energy of concrete with given maximum compressive strength and maximum aggregate size are provided in CEB (1993). For concrete with the maximum compressive strength of 55.2 MPa and maximum aggregate size of 6.35 mm, a specific fracture energy of  $9.3 \times 10^{-5}$  kN/mm is specified, which gives a crack opening width value ( $w$ ) of 0.03 mm for the zero tensile strength point ( $f_t$  taken equal to 10% of  $f'_c$ ). The new model using the Winfrith material model for

concrete is referred to as FE–W in this paper, where W refers to Winfrith.

Fig. 5(a) shows the results from the cyclic loading analysis of the FE–W model of Specimen S1. The steel material was modeled using a bilinear behavior with kinematic hardening (called plastic kinematic material model in *LS-DYNA*) similarly to the FE–CDP and FE–CDP–DS models built in *ABAQUS*. Results from the FE–W model are in accordance with the experimental curves with considerable accuracy. The accuracy of the results showed that the crack simulation capabilities of the concrete material were effective in capturing the true behavior of CFDST column. The FE–CDP model required the insertion of a discrete crack (as done in the FE–CDP–DS model) to fully capture the effects of tensile crack opening and closing in concrete structures.

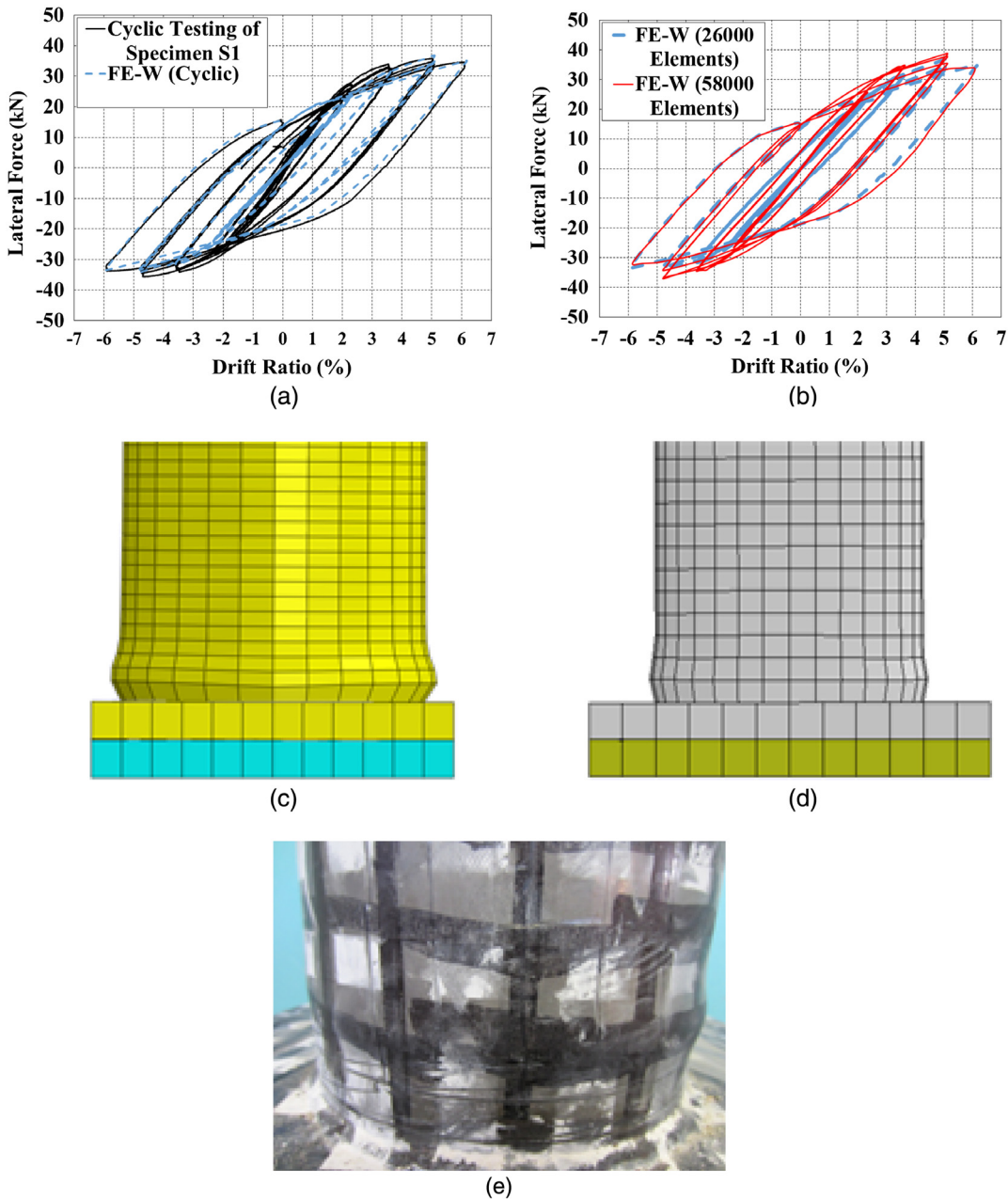


**Fig. 5.** Numerical simulation of the cyclic loading of Specimen S1: (a) lateral force versus drift ratio results from the FE–W model; (b) mesh-sensitivity results from the FE–W model; (c) local buckling (FE–CDP–DS); (d) local buckling (FE–W); (e) local buckling (test)

An additional *LS-DYNA* analysis was conducted to check the sensitivity of the results to the mesh size. Fig. 5(b) shows the results for two similar FE-W models with of Specimen S1 with about 26,000 and 58,000 elements, respectively. The difference between the two sets of hysteresis curves is marginal, confirming convergence of the FE analysis results.

In terms of deformations, both the FE-CDP-DS and FE-W models were able to capture the local buckling of the outer tube near the fixed base. Figs. 5(c-e) show the final deformed shape of the lower end of the column from both analyses, along with a photo from the cyclic testing of Specimen S1. The FE-CDP-DS model [Fig. 5(c)] shows larger deformations in the buckled region, which is in agreement with the more severe pinching, seen in the hysteresis curves of Fig. 4. Results from the FE-CDP-DS model could have been improved by calibrating the inserted crack parameters, but this was not investigated.

### Push-Over and Cyclic Loading Analysis of Specimen S2

Fig. 6 shows the results from the push-over and cyclic loading analyses of Specimen S2 using both the FE-CDP-DS and the FE-W model. The applied cyclic displacement time-history was modified to match the corrected values recorded from the second cyclic test. The push-over analysis provided an acceptable replication of the experimental results in terms of the initial stiffness and maximum lateral resisting force. For cyclic loading, the FE-CDP-DS model captured the strength degradation at cycles with drift amplitudes of about 5 and 6.3%, but (similarly to Specimen S1) exhibited relatively more severe pinching of the numerical hysteresis curves compared to test results. The analysis conducted using the FE-W model provided a more accurate match of the experimental data, as shown in Fig. 6(b).

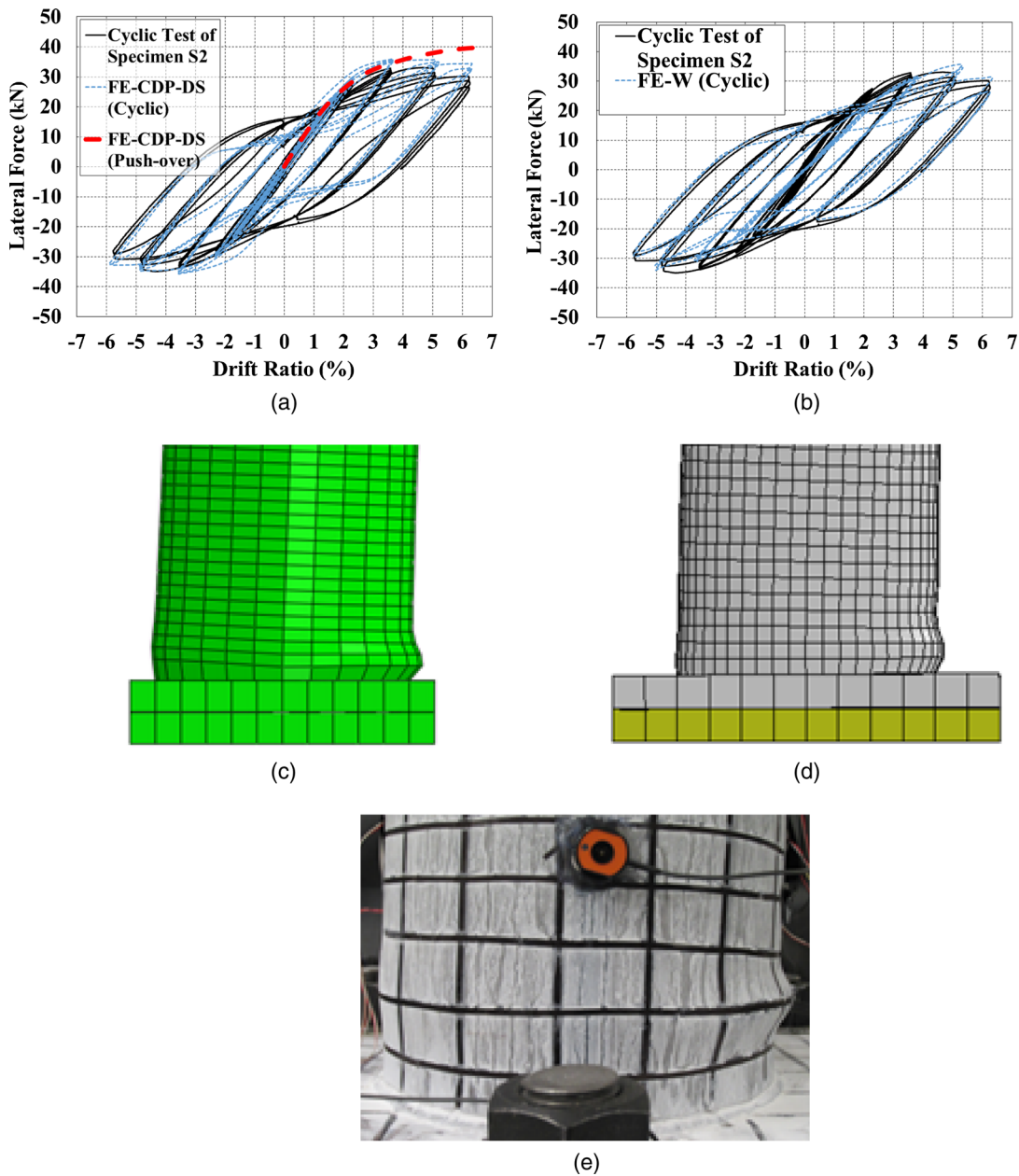


**Fig. 6.** Numerical simulation of the cyclic loading of Specimen S2: (a) results from pushover and cyclic loading analysis using FE-CDP-DS model; (b) results from cyclic loading analysis using FE-W model; (c) local buckling (FE-CDP-DS); (d) local buckling (FE-W); (e) local buckling (test)

Figs. 6(c–e) show the local buckling of the outer tube for Specimen S2 from numerical simulation (FE–CDP–DS and FE–W) and experiments at the end of the test with zero lateral load and a 3.9% residual drift. Resulting deformed shapes are in good agreement. The final results from the FE–CDP–DS analyses of Specimens S1 and S2 under cyclic loading were used as initial conditions for the numerical simulation of fire tests.

## Simulation of the Fire Tests

### Finite-Element Models

This section presents results of the series of thermal-stress analyses performed to simulate the three standard ASTM E119-12a (ASTM 2012) fire tests conducted on Specimens S1–S3. Instead of conducting a fully coupled thermal stress analysis, the simulation was divided into two sequentially coupled parts, referred to as the (1) heat transfer analysis, and (2) stress/deformation analysis. Previous studies have shown that the less computationally intense sequentially coupled analysis provides acceptable results (Hong and Varma 2009; Espinos et al. 2010). An additional fire simulation analysis conducted using the fully coupled method to verify this observation did not give significantly different results (Imani 2014 provides details).

The thermal and structural temperature-dependent material properties for both steel and concrete were adopted from the Eurocode 4 (CEN 2005) specifications. The recommended properties were shown to provide acceptable results for the simulation of CFST columns under fire, with the concrete model being slightly conservative (Espinos et al. 2010). The concrete core was modeled using eight-node solid elements in both heat transfer and stress/deformation analyses. The steel tube was modeled with different types of elements (eight-node solid or four-node shell, in different analyses), as explained in a subsequent paragraph. Fire testing results are first presented for the undamaged Specimen S3, then the moderately and highly damaged columns (Specimens S1 and S2).

### Specimen S3, Undamaged

#### Heat Transfer Analysis

A transient heat transfer analysis was conducted on the undamaged Specimen S3 to simulate the effects of the ASTM E119-12a (ASTM 2012) standard fire test. The recorded time-history of temperature for the outer tube was provided as input for the heat transfer analysis by setting a boundary condition on the outer surfaces of the model (to eliminate possible errors if the furnace air temperature data is used to predict the temperature on the surface of the outer tube). Two heat transfer mechanisms [(1) conduction, and (2) radiation] were defined for the steel–concrete interface. The conduction mechanism was defined based on an average conduction factor, so-called gap conductance, selected to account for the possible gaps between the steel and concrete surfaces. Parameters and constants used for the heat transfer mechanism are presented in Table 1.

Fig. 3(b) shows the FE model of Specimen S3 and the results of the heat transfer analysis for a section at midheight of the column. The colors of the contour lines show the difference in temperature levels going from the outer tube towards the inner tube of the column. This model contains the additional built-up box at the base of the specimen as it was designed and built in the experimental setup. This was done because the bottom end of the inner tube was connected with the bottom plate of the additional built-up box section, providing an all-steel heat-transfer load path to the inner tube at that

location (acting like a so-called short circuit for direct transfer of the thermal energy).

A similar so-called short circuit exists at the top end of the column (even though the top plate was not welded to the inner tube, it was most likely in contact during the test). To investigate the significance of those effects on the heat transfer analysis results, an additional analysis was conducted on the same model in which the thermal connectivity of the built-up box section and the top plate to the bottom and top ends of the inner tube was eliminated.

Fig. 7(a) shows the results of these heat transfer analyses for two different nodes, located at midheight and close to the top end of the inner tube, for the cases with and without the thermal connectivity of the top and bottom plates to the inner tube. Temperature time-history recorded for the inner tube of Specimen S3 during the first fire test is also plotted for comparison [Fig. 7(a)]. The thermocouple was located on the outer surface of the inner tube about 300 mm (12 in.) from its top end. Results indicate that the thermal connectivity of the inner tube to the plates at its top and bottom ends does not significantly affect the nodal temperature values at locations close to the midheight of the inner tube, but does significantly affect results for the nodes located about 0–300 mm (0–12 in.) from the top plate of the specimen [Fig. 7(a)]. After accounting for the special conditions at the top end of the inner tube, the curve obtained for the temperature time-history of the inner tube became closer to the experimental results on average. The FE analyses revealed that the region affected by the so-called short circuit is limited to relatively short portions of the specimen close to its top and bottom ends. To simulate the test conditions, the case with steel end-plates was used in all of the subsequent analyses. The removal of these plates, which are experimental artifacts, would generally improve the fire resistance of the column.

Figs. 7(a and b) show results of the recorded time-history of temperature from the thermocouples installed in the middle of the concrete layer and on the outer surface of the inner tube, along with the results from heat transfer analysis for two selected nodes located approximately at the same positions. The temperature time-history of the outer tube (applied as a boundary condition to the model) is also included in Figs. 7(a and b) for comparison purposes. Figs. 7(a and b) indicate that the numerical simulations have reasonably predicted the temperature time-histories for nodes both in the midwidth of the concrete section and on the inner steel tube.

The fluctuations in temperature values recorded by the thermocouples (especially on the inner tube) do not appear in the numerical results. Analytically, since the temperature values for the concrete and the inner tube increase over time because of the gradual transfer of thermal energy through the defined heat transfer mechanisms over homogeneously defined materials, a smooth increase in temperature values is expected. However, no specific mechanism was modeled to replicate the recorded fluctuations that

**Table 1.** Thermal Constants and Parameters Used in Heat Transfer Modeling

Parameter	Definition	Value
$h$	Coefficient of convection at exposed surface	25 W/m <sup>2</sup> K
$\varphi$	Configuration factor for radiation at exposed surface	1
$\sigma$	Stephan–Boltzmann constant	$5.67 \times 10^{-8}$ W/m <sup>2</sup> k <sup>4</sup>
$\epsilon_m$	Emissivity of exposed surface	0.7
$\epsilon_f$	Emissivity of fire	1
$T_0$	Initial temperature	20°C
$k_{\text{gap}}$	Average gap conductance	200 W/m <sup>2</sup> k

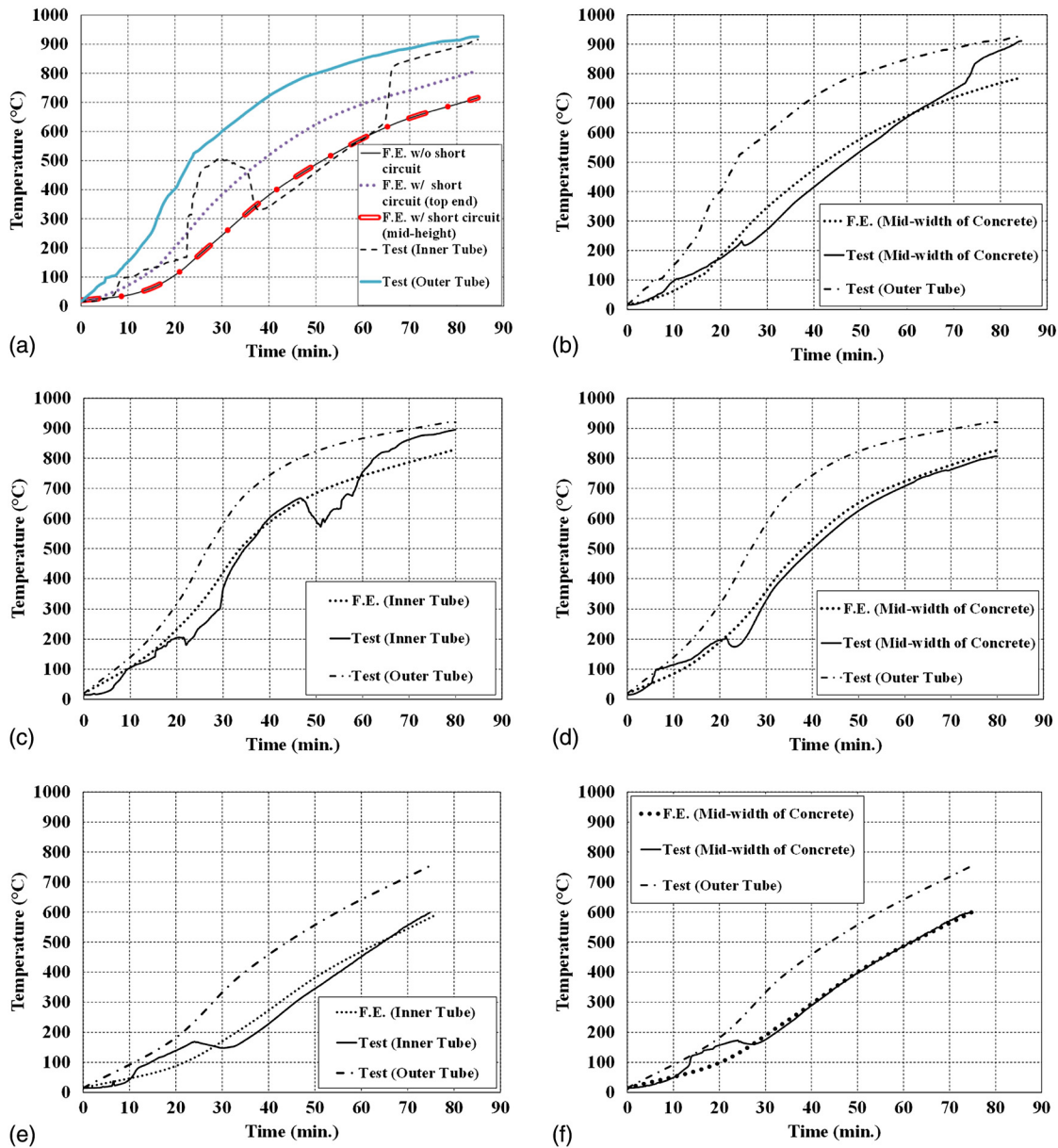


**Fig. 7.** Heat transfer analysis results for various specimens: (a) Specimen S3 inner tube; (b) Specimen S3 midwidth of concrete layer; (c) Specimen S1 inner tube; (d) Specimen S1 midwidth of concrete layer; (e) Specimen S2 inner tube; (f) Specimen S2 midwidth of concrete layer

are possible due to localized pressure build-up and release around concrete aggregates inside the tube as water vapor migrates to the specimen's release holes, which can create nonlinear paths for the heat, alter the trend of temperature distribution, and allow temperatures of the inner tube to fluctuate and reach values exceeding that of the concrete for short periods during the fire test.

Another difference seen between the numerical results and the experimental recordings occurs during the last 15 min of the fire test. The experimental data show that temperature of both the inner tube and the concrete increase more rapidly (to reach the temperature of the outer tube) in the last quarter hour of the test, while the analysis results indicate temperature increasing at the same rate throughout the test and maintaining a proportional difference with the temperature of the outer tube until the end of the test. The sharp increase in the temperature values of the thermocouples in the concrete core and on the inner tube seems to have occurred because of the excessive deformations during the final minutes of the test, which have probably opened a path for the heat to reach both of the

mentioned thermocouples, increasing their temperature values up to that of the outer tube.

### Stress/Deformation Analysis

The FE model used for the heat transfer analysis of Specimen S3 was modified for the stress/deformation analysis, while keeping the geometry and mesh size fixed. The eight-node 3D heat transfer elements were changed to eight-node 3D stress solid elements (i.e., C3D8 R) for both the steel and concrete parts. The mesh size was defined considering both heat transfer and stress/deformation analyses [e.g., Fig. 3(b) shows that a smaller mesh size was selected for the top end of the column, where local buckling of the outer tube was expected to occur as observed in the test]. A Static general analysis was defined with two steps, as follows: (1) applying the external axial load and self-weight load of concrete and maintaining them for the rest of the analysis, and (2) simulating the fire test by applying the results of the heat transfer analysis (time-history

of temperature distribution during the fire exposure for all of the nodes) to the model.

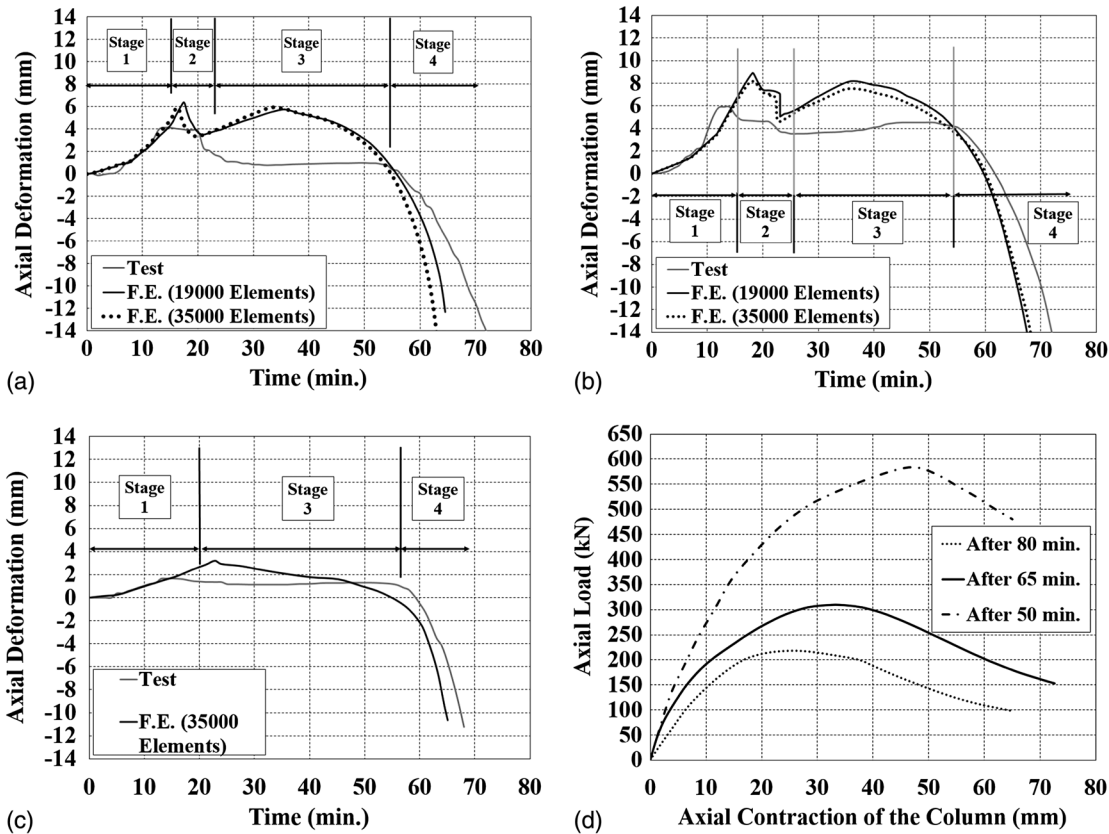
Temperature-dependent thermal and structural properties of steel and concrete materials were adopted from the specifications in the Eurocode 4 (CEN 2005), and used in the elastic-plastic and damaged plasticity models for steel and concrete. The analysis was defined to account for geometric nonlinearities to capture the probable buckling in the model. An initial imperfection consisting of the first buckling mode shape of the column (global buckling) with a displacement amplitude of  $L/1,000$  was imposed on the model to trigger global buckling when the degradation in material properties reach the critical level. No initial imperfection was imposed on the model to initiate local buckling, since the model was shown to be capable of triggering local buckling based on the conditions that are imposed to the elements throughout the analysis (e.g., boundary conditions, constraints, and high plastic strains).

In terms of boundary conditions, the top plate of the column was defined to be fixed. The bottom end was free to move in the axial direction and rotate in the weak direction (one direction had more flexural strength because of the connection to the test frame). The bottom end connection in the test furnace was not completely free to rotate (due to its partial rigidity). An attempt to simulate the effects of the partially fixed connection at the bottom end of the furnace, which had unknown properties, was contemplated, but not done because it was considered that the additional analysis complexities were not necessary to be able to interpret the results in the current context. Modeling with a pinned end results in a reduction of the critical buckling load, thus slightly reducing the fire resistance, and allows for slightly larger rotations as opposed

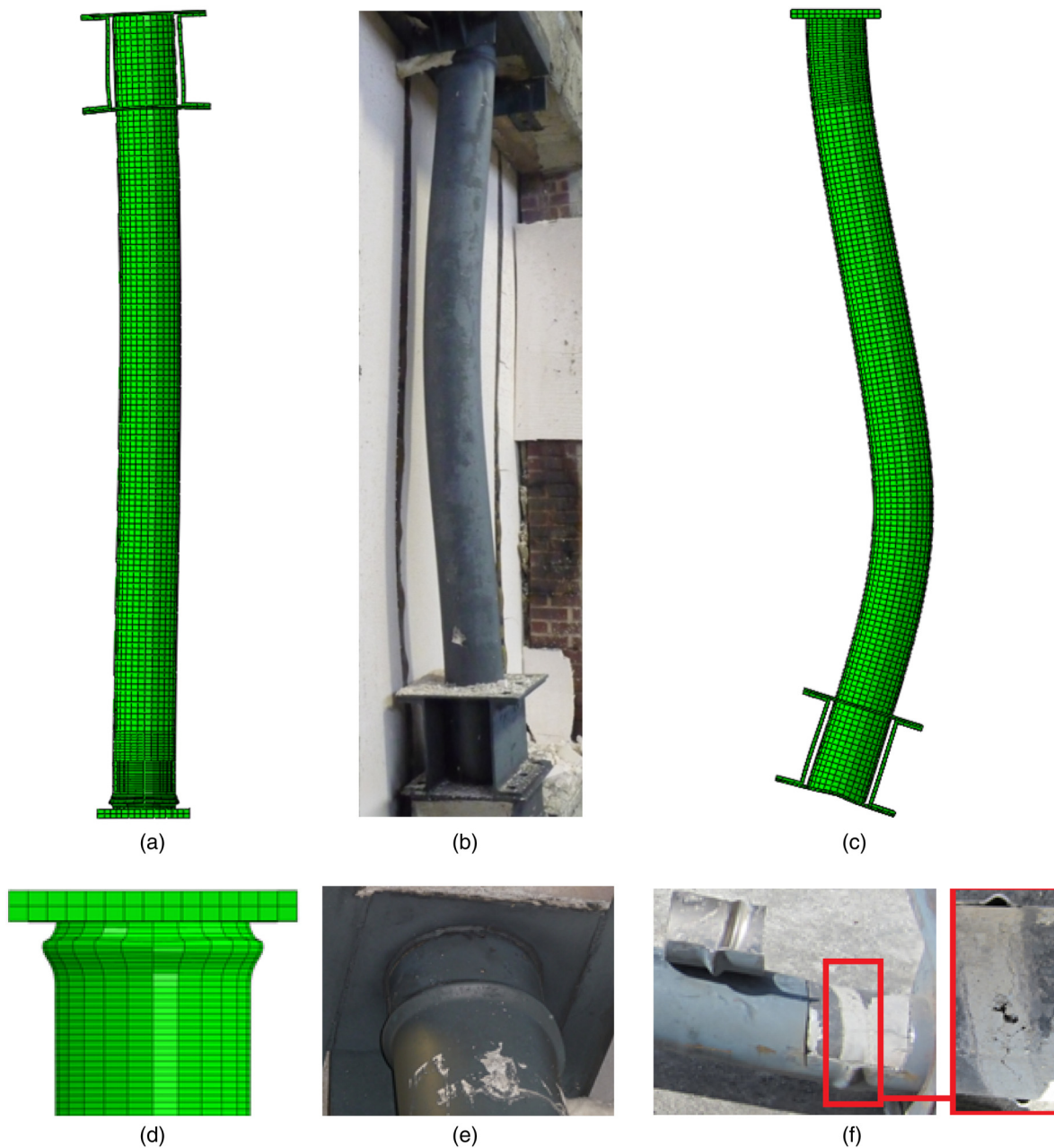
to the experimental results. These changes are considered in the interpretation of the simulation results. The axial loads consisted of the 311 kN external gravity applied as a pressure to the bottom plate of the column and the weight of the concrete core applied as a downward force.

Fig. 8(a) shows the *ABAQUS* analysis results for the axial deformation time-history (extension/contraction) of Specimen S3 during its exposure to the ASTM E119-12a (ASTM 2012) fire. Results from FE analysis are plotted along with the experimental curve. Numerical results follow the same four-stage pattern seen in the experimental results [Fig. 9(a)] consisting of four stages, as follows: (1) expansion of the outer tube (the first ascending branch of the curve), (2) local buckling of the outer tube (the first descending branch of the curve), (3) second phase of expansion/maintaining the axial deformation, and (4) global buckling.

Fig. 8(a) shows that experimental and numerical results are in good agreement in terms of maximum axial deformation and fire resisting time (about 60 min). A noticeable difference between the test and analysis results is the trend in the increase and decrease of the axial deformation, especially during Stage 2 while the outer tube contracts (i.e., the first descending branch of the curve). The sudden drop in the total axial deformation values due to the local buckling of the outer tube was more severe in the tested column compared to the FE model. The analysis captures the local buckling at the right place and time, but showed slightly less severe buckling deformation compared to the test results. Also in Stage 3, when the steel tubes and concrete core are sustaining the axial load together (after a short period during which the whole load was on the outer steel tube), the simulation results show more expansion than the test results, whereas the tubes and concrete



**Fig. 8.** Axial deformation results from the FE simulation of fire tests: (a) time history for Specimen S3; (b) time history for Specimen S1; (c) time history for Specimen S2; (d) axial load versus axial deformation for Specimen S3



**Fig. 9.** Postfire deformed shape of Specimen S3: (a) failure in force-controlled analysis; (b) failure in displacement-controlled analysis; (c) failure in test; (d) simulated local buckling; (e) local buckling from test (first view); (f) local buckling from test (second view)

had only a slight expansion and maintained the same level of axial deformation until the last stage of the test. The second phase of expansion, seen in the numerical results, is considered to be logical because the temperature continues to rise and even though further expansion of the outer tube may only contribute to making the local buckling more severe, there is no mechanism to prevent the concrete core from expanding. However, considering the fact that displacements during the tests were obtained by manual readings from two mechanical gauges, the match between the recorded values and numerical simulation results was deemed to be sufficiently accurate for the purposes of the research reported in this paper.

An additional analysis was conducted on a similar model with a refined mesh size in order to check the mesh sensitivity issue. Results shown in Fig. 8(a) verify the convergence of the FE

analysis for the initial mesh size. The simulation results could have been improved to provide a better match to the experiment by arbitrarily calibrating a few modeling parameters (e.g., the temperature dependent coefficient of thermal expansion for both steel and concrete materials). Nevertheless, since the model was shown to be capable of simulating the four stages defined for the experimental results and provided an acceptable prediction of the fire resisting time, such arbitrary modifications for the specific problem at hand (but that cannot be justified to be generally applicable) were deemed unnecessary for the purposes of the research reported in this paper.

Figs. 9(a and b) show the final state of the numerical model after the termination of the analysis due to the global buckling of the column, with a photo taken at the end of the fire testing of Specimen S3. Global buckling was triggered by the initial imperfection

in the numerical model, but large buckling deformations could not be obtained with the force-controlled analysis approach used. The constant axial load was applied to the column at the beginning of the analysis and maintained during the fire simulation. As the column reached the point when it could no longer sustain the axial load, the force-controlled analysis terminated.

As shown in Fig. 8(a), despite being incapable of simulating the postbuckling phase of the test (after the initiation of global buckling), the analysis was able to replicate the axial deformation of the column and to predict the fire resisting time. To study the behavior of the numerical model in the postbuckling phase, an additional analysis was conducted on the same column in two steps, as follows: (1) the model of Specimen S3 was subjected to the same fire curve up to the point when global buckling was initiated in the previous analysis (about 65 min), and (2) the column end was pushed, so to speak, to apply a compressive load in a displacement-controlled mode (allowing it to go through large buckling deformations). Fig. 9(c) shows the resulting buckled shape of Specimen S3. Recall that the bottom end of the column was modeled as a pinned connection (as opposed to the actual semirigid connection in the test setup) and shows a larger rotation compared to the experimental results [Fig. 9(b)]. Fig. 8(d) shows the axial force versus axial deformation of the column obtained when performing the above displacement-controlled analysis after the column was exposed to the first 50, 65, and 80 min of the standard ASTM E119-12a (ASTM 2012) fire curve. The case with the 65-min fire exposure buckled under an axial load of 307 kN, which is close to the 311-kN load applied during the experiment. For longer periods of fire exposure, the column buckles under lower axial load levels.

Figs. 9(a, d, and e) show the numerical and experimental local buckling of the outer tube close to the top end of the column for Specimen S3. Results indicated that applying the weight of the concrete as a constant force pushing it towards the bottom plate was effective in keeping the bottom end surface of the concrete core in contact with the bottom plate throughout the analysis. Considering this configuration, the expansion of the outer tube could only cause the separation of the top end surface of the concrete core from the top plate of the column. This forced local buckling to occur only at the top end of the specimen, similarly to what occurred in the test. Based on calculations, the weight of the concrete core was enough to overcome the friction resistance between the steel tubes and concrete core.

Comparing Figs. 9(d and e), during the test, local buckling of the outer tube occurred at a lower position than predicted by the simulation results. This difference may be due to the fact that the top steel plate of the column was anchored into the concrete using four 14-mm (0.5-in.) threaded rods [400-mm (16-in.) long] during construction. Threaded rods were not used at the bottom end of the column. Cutting open the steel outer tube after the tests revealed that a short segment of concrete [about 200-mm (8-in.) long] remained uncracked and tied to the top plate. Fig. 9(f) shows the locally damaged end of the column where the outer steel tube was cut to expose the concrete core. A thin crack is seen on the concrete surface at the same location where local buckling of the outer tube occurred. It is inferred that after the initiation of local buckling, further thermal expansion amplified the amplitude of the local buckle. In the numerical simulation, the threaded rods were not modeled, which may explain why, in that case, the separation occurred at the interface of the top end of the concrete and the top plate. Models including the threaded rods were not attempted, as this slight difference in local buckling location was deemed to be of no significance on the specimen behavior.

## Specimen S1, Moderately Damaged

### Heat Transfer Analysis

The same model (built for Specimen S3) was used to conduct the heat transfer analysis of Specimen S1. The boundary condition defined for the surface of the outer tube was modified to follow the recorded time-history of the temperature for the exposed surface of Specimen S1 during the second fire test. Figs. 7(c and d) show the results of the recorded time-history of temperature from the thermocouples installed in the middle of the concrete layer and on the outer surface of the inner tube, along with the results from heat transfer analysis for nodes at the corresponding locations. The temperature time-history of the outer tube (applied as a boundary condition to the model) is also included in both figures for comparison purposes. Figs. 7(c and d) indicate that numerical analysis provided acceptable predictions of the time-history of temperature at both of the selected locations. Similarly to Specimen S3, fluctuations in the time-history of temperature values recorded by the thermocouples were not replicated by the numerical results as the models considered cannot capture this kind of irregular behavior.

### Stress/Deformation Analysis

The FE model of Specimen S1 was subjected to the two-step thermal stress analysis [(1) force-controlled axial loading, and (2) fire simulation] with an initial imperfection created by cyclic lateral loading (ending with a 1.4% residual drift), to simulate the scenario that had occurred for the fire testing of the moderately damaged specimen. The applied initial condition consisted of a stress-free model which had only the residual deformations of the cyclic loading from the previous analysis. Although residual stresses in internal equilibrium could have resulted from the non-linear cyclic loading, those were ignored to avoid complexities at this stage of simulations for the moderately damaged specimen. A more sophisticated approach is considered for the highly damaged column.

Fig. 8(b) shows the time-history of axial deformation for Specimen S1 obtained from the *ABAQUS* analysis, along with the experimental results. Analysis results are in good agreement with test data in terms of the general response pattern, peak axial deformation. The analysis predicted a fire resistance time that was slightly shorter than recorded during the test. Considering that the final failure of the column is controlled by global buckling, modeling the connection of the column to the bottom beam as a pinned end in the out of plane direction (as opposed to the partially fixed condition observed in the test) might have played a role in the prediction of a shorter resistance time by the analysis.

Fig. 8(b) also shows an additional curve derived from an analysis on a similar model with a refined mesh size, which was conducted to check the mesh sensitivity of the results. The marginal difference between the curves indicates the convergence of the FE analysis results. Fig. 10 shows the resulting deformed shape of the Specimen S1 model, which includes the initiation of global buckling of the column, local buckling of the outer tube at the top end (caused by the fire test), and local buckling of the outer tube at the bottom end (cause by cyclic loading of the column). Simulation results are in good agreement with photos from experiment. Similarly to Fig. 9(a) of Specimen S3, Fig. 10 only shows the initiation of the global buckling for Specimen S1, because the force-controlled analysis could not continue to larger deformations. Repetition of the deformation-controlled buckling analysis conducted for Specimen S3 [Figs. 9(c) and 8(d)] was considered unnecessary. Local buckling at the top end of Specimen S3

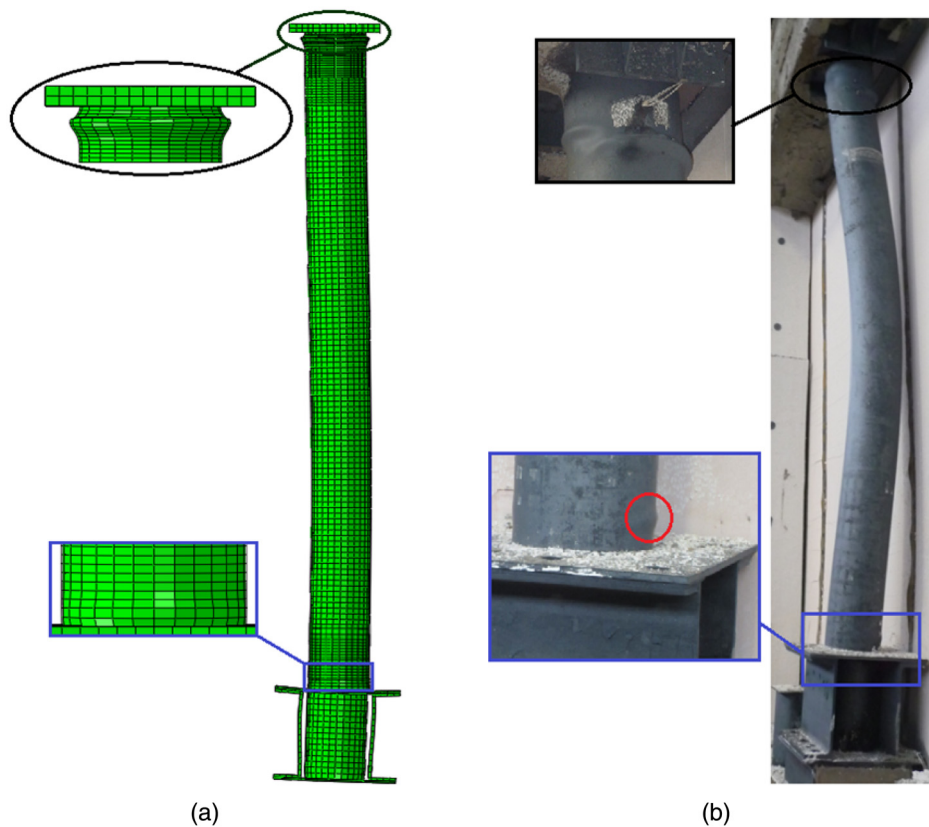


**Fig. 10.** Postfire deformed shape of Specimen S2: (a) simulation results (*ABAQUS*); (b) test results

occurred at a lower height in the test, for the same reasons as for Specimen S1.

### **Specimen S2, Highly Damaged**

#### **Modification of the Model**

Considering the higher severity of seismic damage in Specimen S2 prior to the fire test, and in an attempt to better simulate the effects of the cyclic loading history on the performance of S2 under fire, the FE model for this specimen was modified as described next. To include all the effects of the cyclic loading history (e.g., residual stresses, strains, deformation, degradations, and so on), an additional analysis step was added to the thermal-stress problem. This configuration was significantly more computationally expensive than the case for the moderately damaged Specimen S1, where the axial loading and fire simulation were started after imposing the stress-free resulting deformations from a previous cyclic load analysis as initial imperfection to the FE model.

In order to reduce computational difficulties, the built-up box section was removed from the FE model, reducing it to the configuration that was used in the simulation of cyclic loading tests. Flexibility of the base was accounted for using an additional base plate connected by the bolt load option in *ABAQUS* as presented previously. The model was also enhanced by inserting a horizontal discrete crack into the concrete core just above the bottom plate of the column (the FE-CDP-DS model was used). The mesh size was refined at the bottom end of the outer tube to better capture the expected local buckling caused by both cyclic and fire loading. Results from the simulations conducted on Specimens S3 and S1 and their mesh-sensitivity analyses were used as guidance in the mesh size selection for the Specimen S2 model.

Two separate models, using the same geometry and mesh size but different element types, were built for the heat transfer and stress/deformation analyses. To better replicate the effects of cyclic loading, the element type for the steel tube sections was changed from eight-node solid, i.e., C3D8R (as it was for the fire test simulations of Specimens S3 and S1), to four-node shell elements, i.e., S4R. Although the solid element was shown to provide reasonably accurate results for the fire simulations of Specimens S3 and S1, the shell element was preferred for Specimen S2 because of the importance of the cyclic loading history, and the ability of the shell element to accurately capture local buckling (and subsequent strength and stiffness degradation), in the previous cyclic testing simulations. As such, the final model was similar to the one built for the cyclic testing simulations [Fig. 3(a)].

#### **Heat Transfer Analysis**

Figs. 7(e and f) show the results from the heat transfer analysis of Specimen S2, conducted by applying the measured temperature time-history of the outer tube as a boundary condition. Temperature curves are shown for nodes in the middle of the concrete section and on the inner tube along with the measured data at the corresponding locations. Analysis results are relatively accurate for both locations. Temperature records from the fire testing of Specimen S2 show less fluctuations compared to the past two tests, thus making a better match with the smooth numerical results.

#### **Stress/Deformation Analysis**

To keep the multistep FE analysis computationally efficient, the cyclic loading step applied only a few displacement cycles (not the full protocol used in the test). The applied displacement cycles were selected to include a few of the drift ratio amplitudes identified in the test protocol, namely cycles at drift ratios of about 3.5, 5,

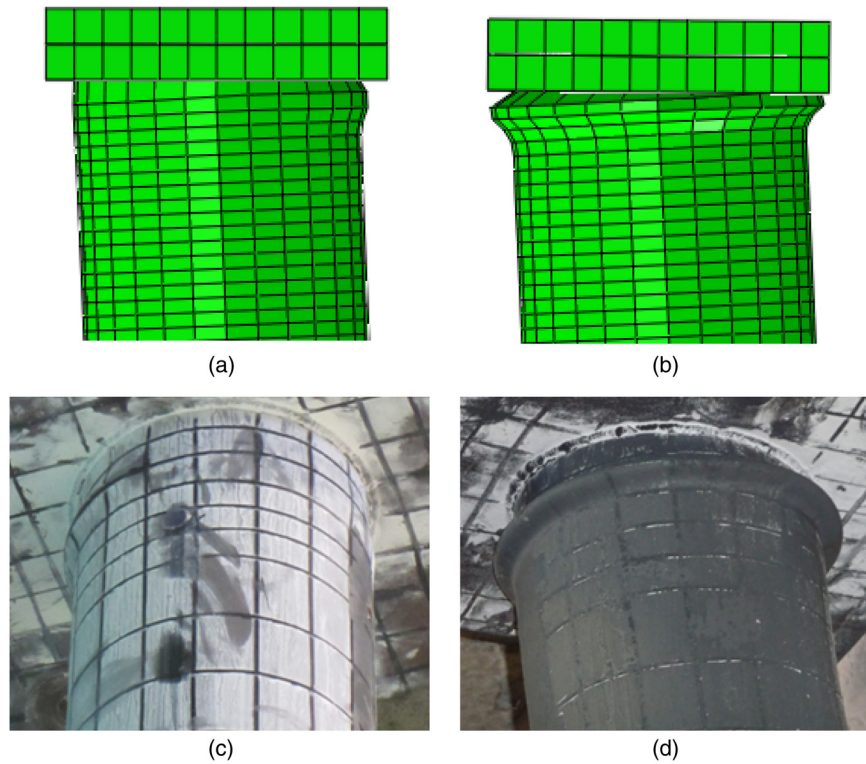


**Fig. 11.** Local buckling of Specimen S2: (a) simulation of prefire condition damage from cyclic loading using *ABAQUS*; (b) simulation of fire-induced damage; (c) specimen before fire test; (d) specimen after fire test

and 6.2% (the 6.2% value is maximum recorded value). Each of these cycles was applied once to create the local buckling effect at the bottom end of the column. An additional cycle at a drift ratio of 6% was applied to the model in the end, to be able unload to a residual drift close to the value recorded in the test (3.9%).

After the cyclic analysis, the column model was then subjected to a two-step thermal stress analysis [(1) axial loading, and (2) fire test] to simulate the effects of the ASTM E119-12a (ASTM 2012) fire on the highly damaged specimen. To replicate the test conditions, a fixed boundary condition was imposed at the locally buckled end of the column, and a pin boundary condition able to translate vertically was modeled at the other end, leaving it free to move in the axial direction and rotate in the direction in which cyclic loading had been applied to the column in the previous step.

Fig. 8(c) shows the time-history of axial deformation for Specimen S2. The numerical model was found to give reasonable predictions of both maximum axial deformation and fire resisting time for the specimen (about 60 min). Similarly to the results for Specimens S3 and S1, the numerical simulation showed a relatively longer expansion period for the outer tube. In terms of the stages defined for the variation of axial deformation versus time, the analysis results seem to more closely match the experimental ones than was the case for the previous specimens, as the sharp expansion and drop from the curve typically corresponding to Stage 2 was not observed in Specimen S2 (contrary to the previous specimens).

Fig. 11 shows the damaged end of the column (caused by cyclic loading) before and after the fire test from both analysis and experimental results. Results show that the analysis successfully simulated the effects of fire testing on increasing the severity of the local buckling, which had been initiated in the cyclic loading step and deliberately positioned at the top end of the furnace in an attempt to combine the damaging effects of seismic and fire loads.

## Conclusions

Finite-element models built for CFDST columns using the general FE software packages *ABAQUS* and *LS-DYNA* were used in attempts to analytically replicate the experimental results obtained for Specimens S1–S3 under both cyclic and fire loads. Initial simulation of the cyclic lateral loading using the damaged plasticity model for concrete provided acceptable predictions of the maximum lateral resisting force, but failed to capture the pinching phenomena observed in the hysteresis behavior of CFDST columns.

Considering the short-comings of the damaged plasticity model in simulating the formation of tensile cracks and the effects of their subsequent opening and closing in concrete structures, the model was modified by inserting a discrete horizontal crack at the location with the maximum tensile stress. The modified model provided a much better replication of the experimental hysteresis curves, and underscored how results can be affected by different strategies adopted for modeling the behavior of concrete in tension when investigating inelastic cyclic behavior.

To further investigate the effects of concrete tensile cracking on the flexural behavior of CFDST columns, an additional FE model was built using the Winfrith concrete model to account for tensile cracks and the effect of their opening and closing. Simulation results showed significant improvements in replicating the experimentally obtained hysteretic results.

Finally, with respect to fire testing simulation, the damaged plasticity with discrete crack model provided acceptable predictions of fire resistance time and of the specimen deformations for different cases of fire tests conducted on damaged and undamaged specimens. The thermal and structural material properties adopted from the Eurocode 4 (CEN 2005) general rules for structural fire design for steel and concrete (in both fire and postfire situations)

were sufficiently accurate to be used for the numerical simulation of the behavior of CFDST columns under fire and postfire cyclic loading conditions.

## References

- ABAQUS [Computer software]. Waltham, MA, Dassault Systèmes.
- ACI (American Concrete Institute). (2011). "Building code requirements for structural concrete and commentary." *ACI 318-11*, Farmington Hills, MI.
- ASTM. (2012). "Standard test methods for fire tests of building construction and materials." *E119-12a*, West Conshohocken, PA.
- Broadhouse, B. J., and Neilson, A. J. (1987). "Modelling reinforced concrete structures in DYNA3D." *Rep. AEEW-M-2465*, UKAEA Atomic Energy Establishment, U.K.
- CEB (Comite Euro-Int. du Beton). (1993). *CEB-FIP model code 1990*, Redwood Books, Trowbridge, U.K.
- CEN (Comité Européen de Normalisation). (2005). *Eurocode 4: Design of composite steel and concrete structures. Part 1.2: General rules—Structural fire design*, Brussels, Belgium.
- Chen, W. F. (2007). *Plasticity in reinforced concrete*, J. Ross Publishing, 474.
- Cousins, W. J., and Smith, W. D. (2004). "Estimated losses due to post-earthquake fire in three New Zealand cities." *Proc., New Zealand Society of Earthquake Engineering (NZSEE) Conf.*, Wellington, New Zealand.
- Espinos, A., Romero, M. L., and Hospitaler, A. (2010). "Advanced model for predicting the fire response of concrete filled tubular columns." *J. Constr. Steel Res.*, 66(8–9), 1030–1046.
- Goto, Y., Kumar, G. P., and Kawanishi, N. (2010). "Nonlinear finite-element analysis for hysteretic behavior of thin-walled circular steel columns with in-filled concrete." *J. Struct. Eng.*, 10.1061/(ASCE)ST.1943-541X.0000240, 1413–1422.
- Goto, Y., Mizuno, K., and Prosenjit Kumar, G. (2012). "Nonlinear finite element analysis for cyclic behavior of thin-walled stiffened rectangular steel columns with in-filled concrete." *J. Struct. Eng.*, 10.1061/(ASCE)ST.1943-541X.0000504, 571–584.
- Hajjar, J. F. (2000). "Concrete-filled steel tube columns under earthquake loads." *Prog. Struct. Eng. Mater.*, 2(1), 72–81.
- Han, L. H. (2001). "Fire performance of concrete filled steel tubular beam-columns." *J. Constr. Steel Res.*, 57(6), 695–709.
- Han, L. H., Tao, Z., Huang, H., and Zhao, X. L. (2004). "Concrete-filled double skin (SHS outer and CHS inner) steel tubular beam-columns." *Thin Wall Struct.*, 42(9), 1329–1355.
- Han, L. H., and Yang, Y. F. (2005). "Cyclic performance of concrete-filled steel CHS columns under flexural loading." *J. Constr. Steel Res.*, 61(4), 423–452.
- Han, L. H., Zhao, X. L., Yang, Y. F., and Feng, J. B. (2003). "Experimental study and calculation of fire resistance of concrete-filled hollow steel columns." *J. Struct. Eng.*, 10.1061/(ASCE)0733-9445(2003)129:3(346), 346–356.
- Hong, S., and Varma, A. H. (2009). "Analytical modeling of the standard fire behavior of loaded CFT columns." *J. Constr. Steel Res.*, 65(1), 54–69.
- Imani, R. (2014). "Post-earthquake fire resistance of ductile concrete filled double-skin tube columns." Ph.D. thesis, State Univ. of New York at Buffalo, Buffalo, NY.
- Imani, R., Mosqueda, G., and Bruneau, M. (2014). "Experimental study on post-earthquake fire resistance of ductile concrete-filled double-skin tube columns." *J. Struct. Eng.*, 10.1061/(ASCE)ST.1943-541X.0001168, 04014192.
- Johansson, M., and Gylltoft, K. (2001). "Structural behavior of slender circular steel-concrete composite columns under various means of load application." *Steel Compos. Struct.*, 1(4), 393–410.
- Kodur, V. K. R. (1998). "Performance of high strength concrete-filled steel columns exposed to fire." *Can. J. Civ. Eng.*, 25(6), 975–981.
- LS-DYNA version smp s R7.0.0 [Computer software]. Livermore, CA, Livermore Software Technology Corporation.
- Lu, H., Han, L. H., and Zhao, X. L. (2010). "Fire performance of self-consolidating concrete filled double skin steel tubular columns: Experiments." *Fire Safety J.*, 45(2), 106–115.
- Lu, H., Zhao, X. L., and Han, L. H. (2011). "FE modelling and fire resistance design of concrete filled double skin tubular columns." *J. Constr. Steel Res.*, 67(11), 1733–1748.
- Mander, J. B., Priestley, M. J. N., and Park, R. (1988). "Theoretical stress-strain model for confined concrete." *J. Struct. Eng.*, 10.1061/(ASCE)0733-9445(1988)114:8(1804), 1804–1826.
- Marson, J., and Bruneau, M. (2004). "Cyclic testing of concrete-filled circular steel bridge piers having encased fixed-based detail." *J. Bridge Eng.*, 10.1061/(ASCE)1084-0702(2004)9:1(14), 14–23.
- Moliner, V., Espinos, A., Romero, M. L., and Hospitaler, A. (2013). "Fire behavior of eccentrically loaded slender high strength concrete-filled tubular columns." *J. Constr. Steel Res.*, 83(4), 137–146.
- NOAA (National Oceanic and Atmospheric Administration). (1972). "A study of earthquake losses in the San Francisco Bay area—Data and analysis." *Rep. Prepared for the Office of Emergency Preparedness*, Washington, DC.
- Sakino, K., Nakahara, H., Morino, S., and Nishiyama, A. (2004). "Behavior of centrally loaded concrete-filled steel-tube short columns." *J. Struct. Eng.*, 10.1061/(ASCE)0733-9445(2004)130:2(180), 180–188.
- Scawthorn, C., Eidinger, J. M., and Schiff, A. J. (2005). *Fire following earthquake*, ASCE, Reston, VA.
- Scawthorn, C. R. (2008). "Fire following earthquake—The shake out scenario report." *SPA Technical Rep.*, SPA Risk, LLC, Berkeley, CA.
- Schwer, L. (2011). "The Winfrith concrete model: Beauty or beast? Insights into the Winfrith concrete model." *Proc., Eighth European LS-DYNA Users Conf.*, Dynamore, Stuttgart, Germany.
- Uenaka, K., Kitoh, H., and Sonoda, K. (2008). "Concrete filled double skin tubular members subjected to bending." *Steel Comp. Struct.*, 8(4), 297–312.
- Usami, T., Susantha, K. A. S., and Ge, H. (2001). "Uniaxial stress-strain relationship of concrete confined by various shaped steel tubes." *Eng. Struct.*, 23(10), 1331–1347.
- Yang, Y. F., and Han, L. H. (2008). "Concrete-filled double-skin tubular columns under fire." *Mag. Concrete Res.*, 60(3), 211–222.
- Zhao, X. L., and Grzebieta, R. (2002). "Strength and ductility of concrete filled double skin (SHS inner and SHS outer) tubes." *Thin Wall Struct.*, 40(2), 199–213.